

A COMPARISON OF DEFORMATION TEXTURES AND MECHANICAL PROPERTIES PREDICTED BY DIFFERENT CRYSTAL PLASTICITY CODES

Craig S. Hartley
El Arroyo Enterprises LLC
Sedona, AZ USA

Paul R. Dawson, Donald E. Boyce
Sibley School of Mechanical and Aerospace Engineering, Cornell University
Ithaca, NY USA

Surya R. Kalidindi, Marko Knezevic
Department of Materials Science and Engineering, Drexel University
Philadelphia, PA USA

Carlos Tomé, Ricardo Lebensohn
MST-8, Los Alamos National Laboratory
Los Alamos, NM USA

S. Lee Semiatin, Todd J. Turner
Air Force Research Laboratory, Materials and Manufacturing Directorate
Wright-Patterson AFB, OH USA

Ayman A. Salem
Universal Technology Corporation
Dayton, OH USA

ABSTRACT

Four crystal plasticity codes, the viscoplastic Material Point Simulator (MPS) developed at Cornell and the ViscoPlastic Self-Consistent code (VPSC7b) developed at LANL, and two elastic-viscoplastic codes developed at Drexel University, were employed to calculate deformation textures and mechanical properties of model polycrystalline specimens by simulating isochoric, free upsetting. Uniaxial compression of a model sample with a starting random texture of 5000 grains was carried out at a constant true strain rate of 0.001/s to a true strain of 1.0 with 0.02 strain increments. Material properties simulated a face-centered cubic (FCC) alloy, Type 304 Stainless Steel, and a hexagonal close-packed (HCP) material, unalloyed Ti. Both non-hardening and linear hardening conditions were investigated. Different strain-rate sensitivities simulated deformation conditions appropriate to ambient and elevated temperature conditions. All codes permitted use of the Taylor homogenization hypothesis, resulting in an upper bound for the mechanical properties. All codes produce essentially identical results for the same input material, homogenization hypothesis and deformation conditions. For comparison, one alternative homogenization hypothesis to model grain interactions was examined for each of the MPS and VPSC7b codes.

INTRODUCTION

Over the last two decades, significant progress in the field of crystal plasticity modeling has led to the development of many codes with proven success in simulating various aspects of the mechanical behavior of both FCC and HCP metals. This proliferation makes it difficult for researchers to decide which code is best suited for a particular application. This study aims to provide an unbiased study of the capabilities and limitations of three different types of codes by examining the results obtained from each using identical input conditions. The codes employed are 1) the ViscoPlastic Self-Consistent code¹ (VPSC7b) developed and maintained by C. Tomé and R. Lebensohn at Los Alamos National Laboratory, Los Alamos, NM, hereafter referred to as V; 2) the Material Point Simulator (MPS) code² developed by P. R. Dawson, D. E. Boyce and associates at Cornell University, hereafter referred to as C; and 3) two elastic-plastic codes, one each for face-centered cubic and hexagonal close-packed metals, developed by S. Kalidindi and associates at Drexel University^{3,4}, hereafter referred to collectively as D.

All of the codes are capable of calculating effective stress-effective strain (SS) curves, the final orientation of each grain in the ensemble (TEX), from which pole figures can be calculated, and the effective Taylor factor (M) for the ensemble. All employ a form of the Voce hardening law for hardening on the active slip systems and the V and D codes permit the inclusion of latent hardening in cases where more than one type of slip system is active. Although all codes are capable of including both slip and twinning in the calculations, only slip was considered in this study to reduce the number of permutations of material variables. A homogenization assumption specifies the relationship between the state of deformation for individual grains and the global state of deformation for the ensemble. The Taylor hypothesis, in which the strain or strain rate in each grain is the same as that for the ensemble, is common to all three codes and gives an upper bound to the resulting SS curve. In addition the C code provides an option for the Sachs hypothesis, in which the state of stress in each grain is the same as for the ensemble, giving a lower bound to the SS curve. Although this code also permits selected weighted averages of the Taylor and Sachs hypotheses, these were not investigated in this study. The Affine linearization hypothesis of the V code⁵ was employed in this work for comparison.

MATERIAL PARAMETERS AND COMPUTATIONAL DETAILS

Material properties employed in the calculations correspond to austenitic stainless steel, a face-centered cubic (FCC) avatar, and unalloyed Ti, a hexagonal close-packed (HCP) avatar. Crystal deformation was confined to $\{111\}\langle 110 \rangle$ slip for the FCC material and to the basal $\langle a \rangle$, first order prismatic $\langle a \rangle$ and pyramidal $\langle c + a \rangle$ systems in the HCP material. For both ambient and high temperature deformation conditions, relative values of the critical resolved shear stress (CRSS) on each of the slip systems in the HCP material were set to 1.0:0.7:3.0, respectively. Deformation by twinning was not included in any of the calculations. Reduced values of the CRSSs on each slip system were employed, so that the CRSS on the reference slip system (basal for hcp) was 1.0.

Different temperatures were simulated only by employing different values of the stress exponent (strain-rate sensitivity) while the hardening ratios and CRSSs remained constant. For both the FCC and HCP materials, high temperature deformation conditions correspond to a stress exponent $n = 4$ and low temperature, to a stress exponent of $n = 20$ in an equation of the form

$$\dot{\epsilon}_{ij}^k = \dot{\gamma}_o m_{ij}^k \left(\frac{m_{rs}^k \sigma_{rs}}{\tau_o^k} \right)^n \quad (1)$$

where $\dot{\epsilon}_{ij}^k$ is the ij^{th} component of the deviatoric strain rate due to slip on the k^{th} slip system, m_{ij}^k is the Schmid tensor on that system, σ_{rs} is the local deviatoric stress tensor, n is the stress exponent, $\dot{\gamma}_o$ is a reference strain rate, and τ_o^k is a reference stress for slip on the k^{th} slip system, respectively. The strain rate due to slip on all systems is obtained by summing equation (1) over all active slip systems. While the V code employs this form of the rate-dependent law, the C and D codes use the form in which the resolved shear stress is given in terms of the strain rate, using a strain-rate sensitivity exponent, $m = 1/n$.

Both hardening and non-hardening conditions were investigated using an empirical Voce-type hardening law. On each active slip system these relationships have the form

$$\tau(\gamma) = \tau_o + (\tau_s - \tau_o) (1 - e^{-\alpha\gamma}) \quad (2)$$

where $\tau(\gamma)$ is the resolved shear stress at a resolved shear strain of γ , τ_o and τ_s are the critical resolved shear stress (CRSS) and saturation stress, respectively on the slip system and α is a hardening parameter. The V code employs a version of equation (2) that uses the accumulated shear strain in a grain instead of γ for the strain and permits hardening to approach a non-zero asymptotic value, introducing a fourth parameter into the expression¹. The present study treats only linear hardening, simulated over the range of strain for which calculations were performed by setting $\tau_s = 1000 \tau_o$ and the initial hardening rate $\theta_o = \alpha(\tau_s - \tau_o) = 0.2\tau_o$. For the HCP material the initial hardening rates on the active slip systems were selected in the same ratios as the CRSSs.

The effective Taylor factor, M , for the ensemble of grains was calculated at each increment of effective strain for the V and D codes. In the former case M is given by

$$M = \frac{\sigma_{ij} \dot{\epsilon}_{ij}}{\sqrt{\sigma_{ij} \sigma_{ij}} \sqrt{\dot{\epsilon}_{kl} \dot{\epsilon}_{kl}}} \quad (3)$$

where summation over repeated indices is implied and the deviatoric stress and strain rate components refer to global values. The SS curves were normalized by dividing stresses by the CRSS on the reference slip system (basal slip for HCP). Equation (3) and the use of 1.0 as the CRSS on the reference slip system results in the value of M being numerically equal to the von Mises effective stress at each increment of strain for both FCC and HCP materials. The D code uses a definition for M that replaces individual stress components in equation (3) with the CRSS on the reference system.

Computations of the SS curves were performed at effective strain intervals of 0.02 from an initial true strain of 0.0 to a final value of 1.0 under uniaxial compression along the x_3 axis at a rate of 10^{-3} s^{-1} . However, because of the elastic-viscoplastic nature of the D codes, when the instantaneous total strain was less than 0.05 it was necessary to perform calculations at a smaller increment of strain than for the rest of the curve to achieve agreement with the purely viscoplastic codes in the vicinity of initial yielding. an ensemble of 5000 randomly oriented grains was selected as the starting material.

RESULTS

Face-Centered Cubic

The SS curves for the FCC calculations produced by all codes are shown in Figure 1. The legend identifying data sets specifies the code (C, D, V), crystal structure (F or H), temperature as high (H) or ambient (R), hardening (H) or non-hardening (N), and the homogenization assumption. The latter is represented by U for the Taylor hypothesis, L for the Sachs and A for Affine linearization. The effective stress is numerically equal to M for the V code.

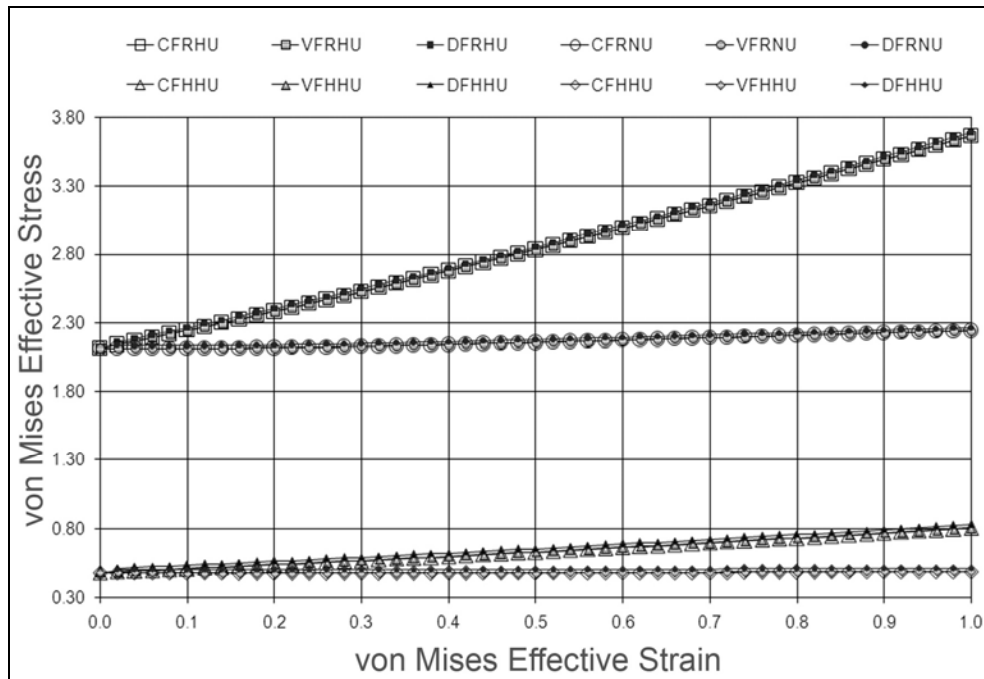


Figure 1. FCC Upper Bound Effective Stress-Strain Curves from All Codes

Pole figures from the calculations shown in Figure 1 are given in Figures 2a and 2b for hardening and non-hardening, respectively, under ambient temperature deformation conditions. Orientations of all grains in the ensemble at an effective true strain of 1.0 were employed to construct pole figures for the deformed materials using TSL⁶ software marketed by EDAX. All pole figures have the compression (x_3) axis at the center of the figure and intensity contours represent multiples of the random probabilities for the indicated poles.

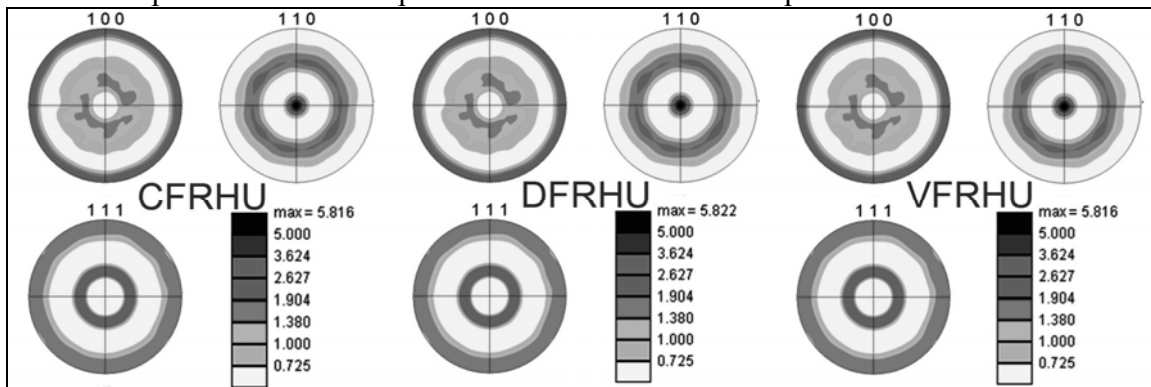


Figure 2a. FCC Pole Figures for Ambient Temperature, Hardening Deformation Condition

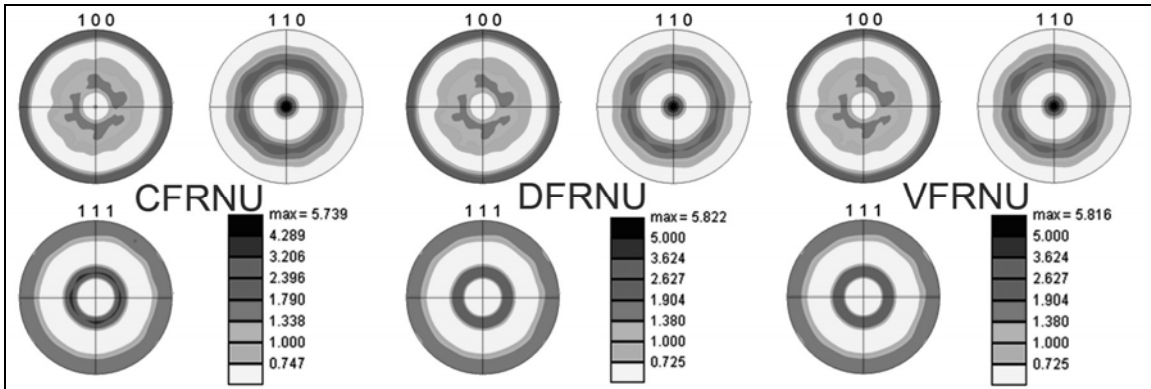


Figure 2b. FCC Pole Figures for Ambient Temperature, Non-Hardening Deformation Condition

Figures 3a and 3b show similar pole figures for high temperature conditions.

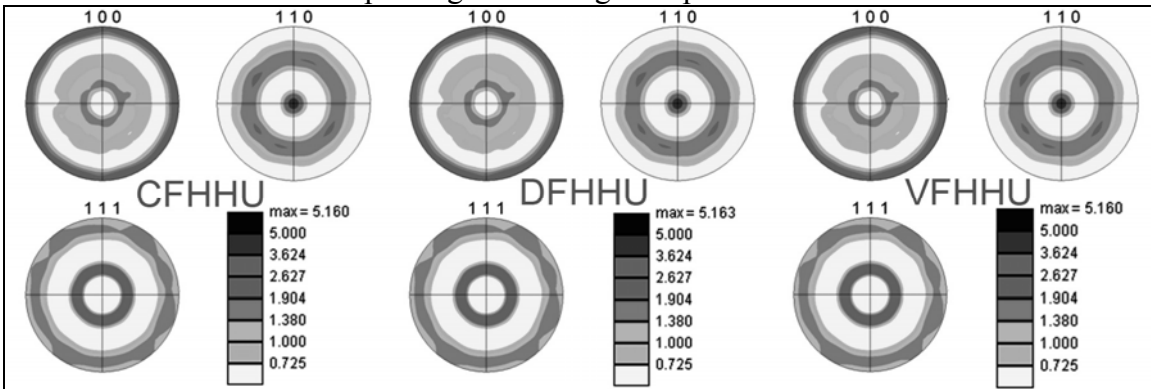


Figure 3a. FCC Pole Figures for High Temperature, Hardening Deformation Condition

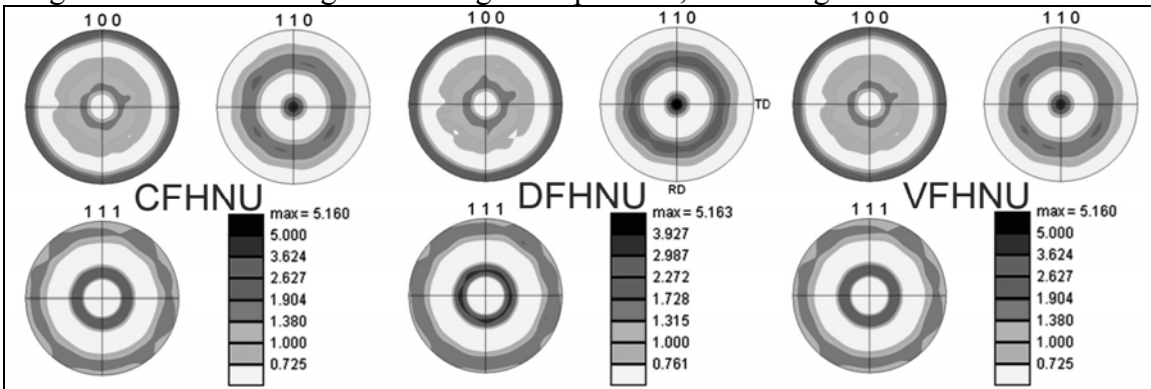


Figure 3b. FCC Pole Figures for High Temperature, Non-Hardening Deformation Condition

Figure 4 compares the SS curves calculated with the C code using the U and L assumptions.

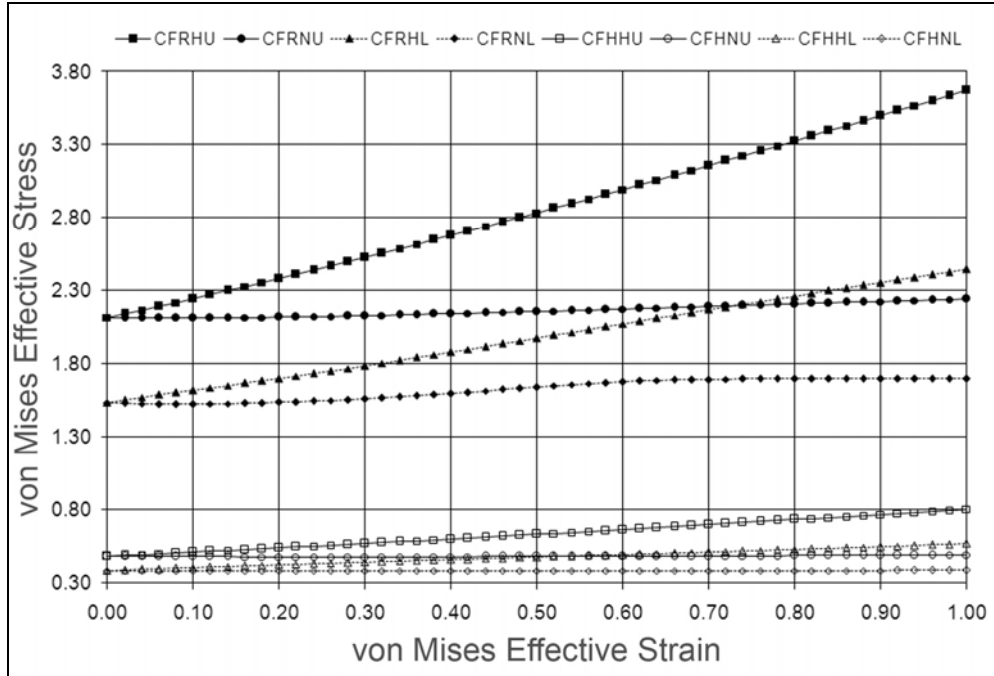


Figure 4. FCC Upper and Lower Bound Effective Stress-Strain Curves from C code

Figure 5 shows pole figures associated with the lower bound stress-strain curves in Figure 4.

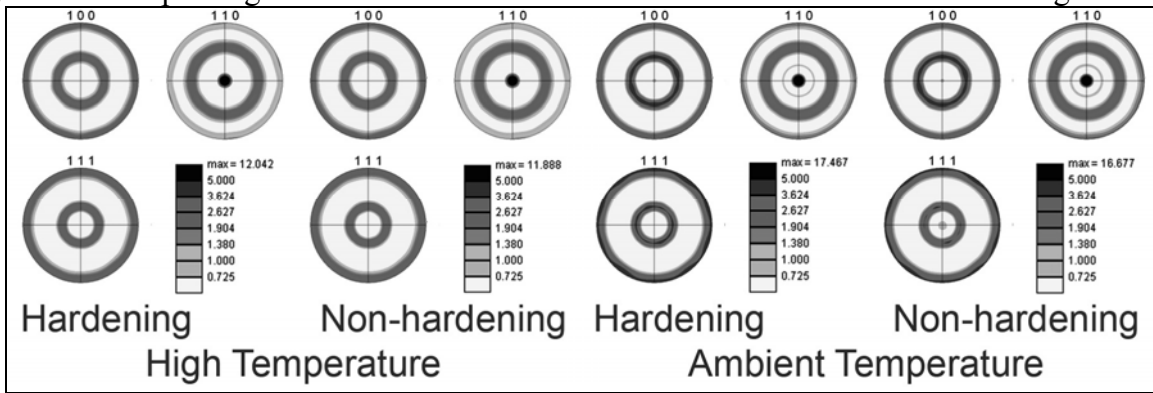


Figure 5. FCC Pole Figures for Lower Bound calculations with C code

Figure 6 compares stress-strain curves obtained with the V code using the Taylor (T) model with the same deformation conditions calculated using the Affine (A) option of the code.

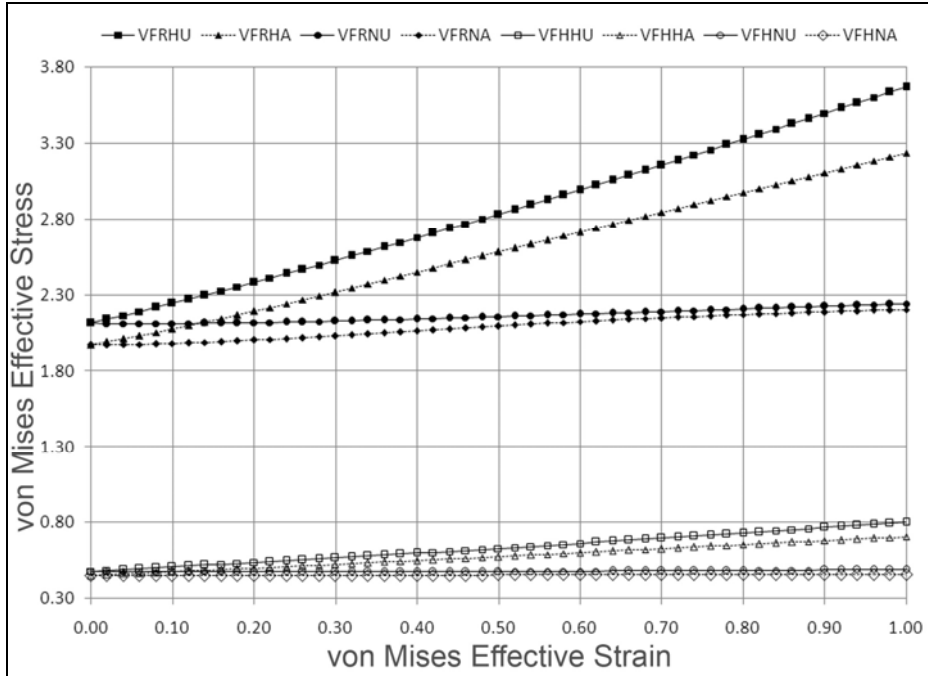


Figure 6. FCC Effective Stress-Strain Curves from Taylor and Affine options of V code

Figure 7 gives pole figures obtained using the Affine option of the V code.

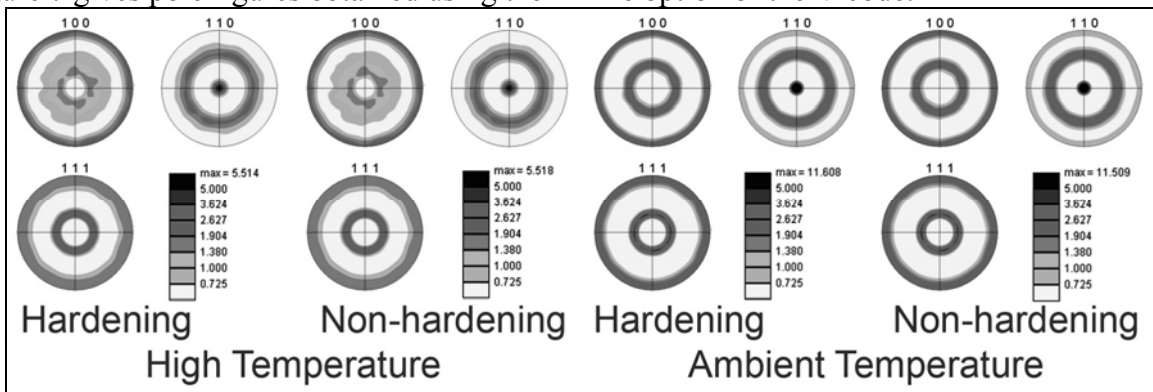


Figure 7. FCC Pole Figures from Affine option calculated with V code

Hexagonal Close-Packed

Figure 8 shows SS curves obtained from all codes for HCP material.

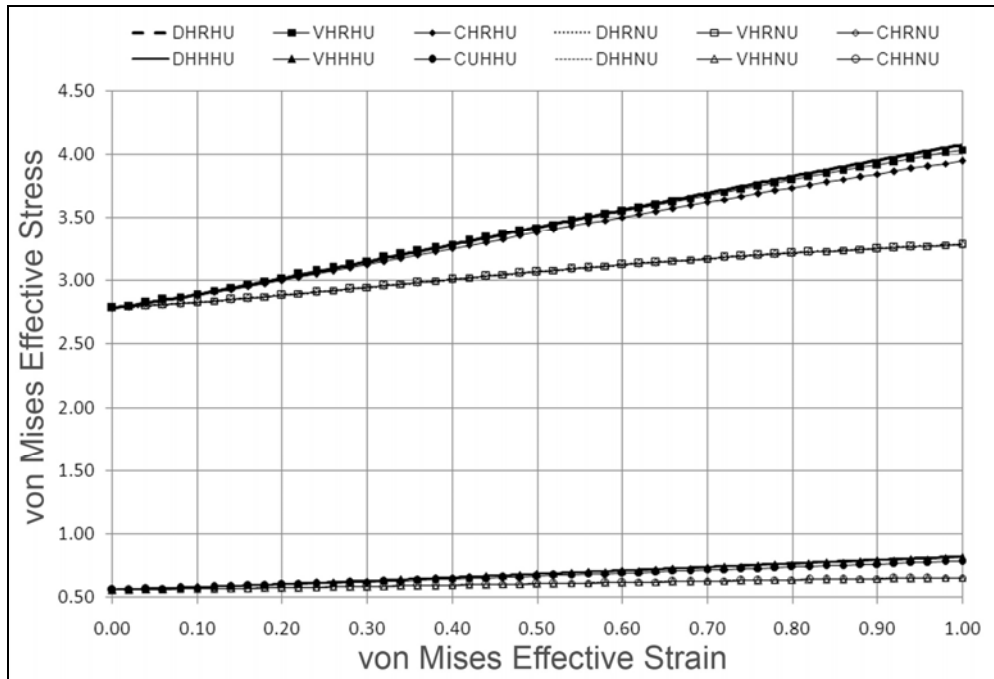


Figure 8. HCP Upper Bound Effective Stress-Strain Curves from all codes

Pole figures for the stress-strain curves in Figure 8 are shown in Figure 9a, 9b, 10a and 10b.

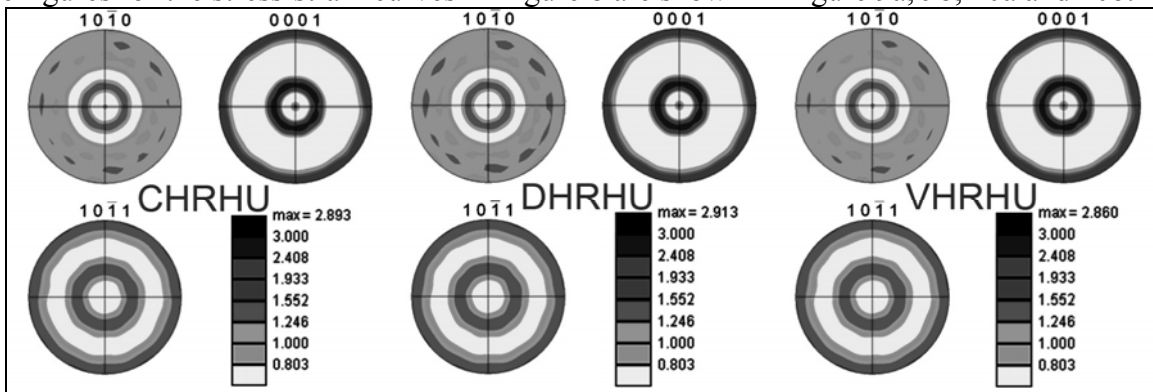


Figure 9a. HCP Pole Figures for Ambient Temperature, Hardening Deformation Condition

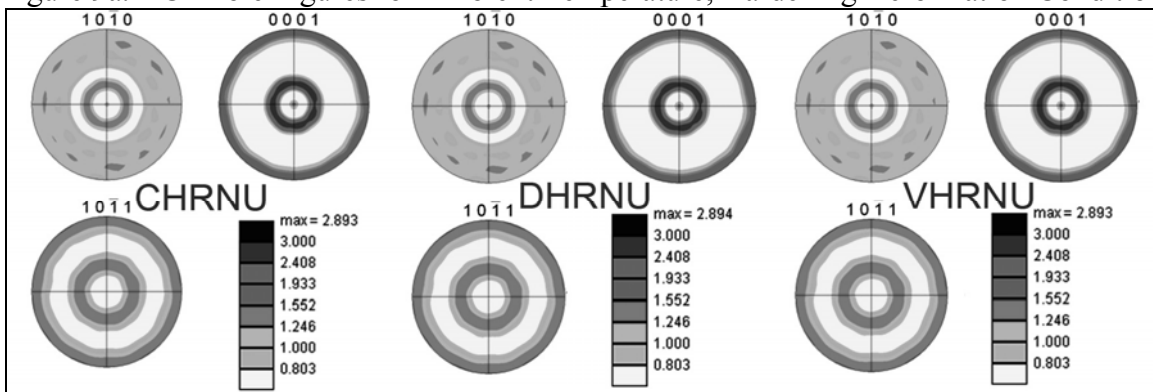


Figure 9b. HCP Pole Figures for Ambient Temperature, Non-Hardening Deformation Condition

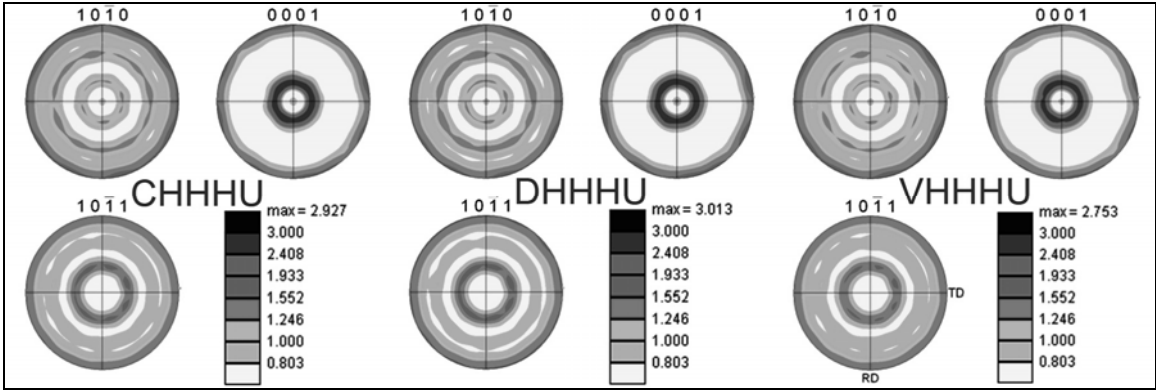


Figure 10a. HCP Pole Figures for High Temperature, Hardening Deformation Condition

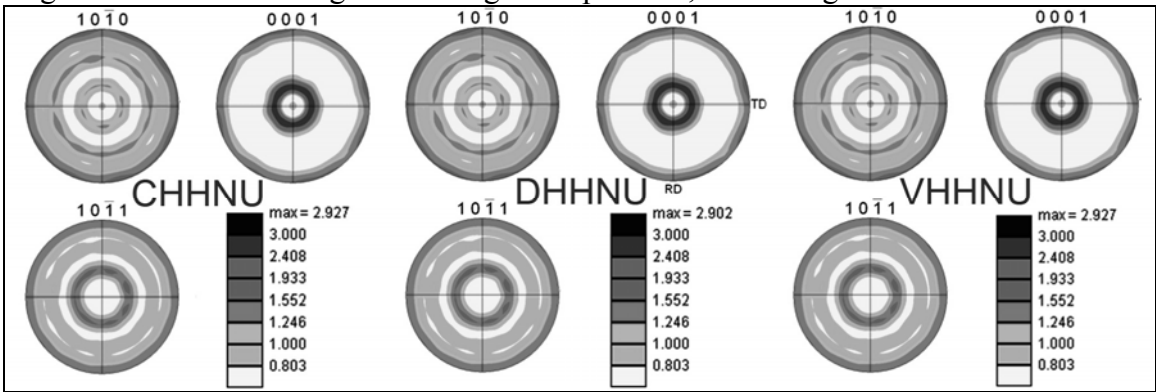


Figure 10b. HCP Pole Figures for High Temperature, Non-Hardening Deformation Condition

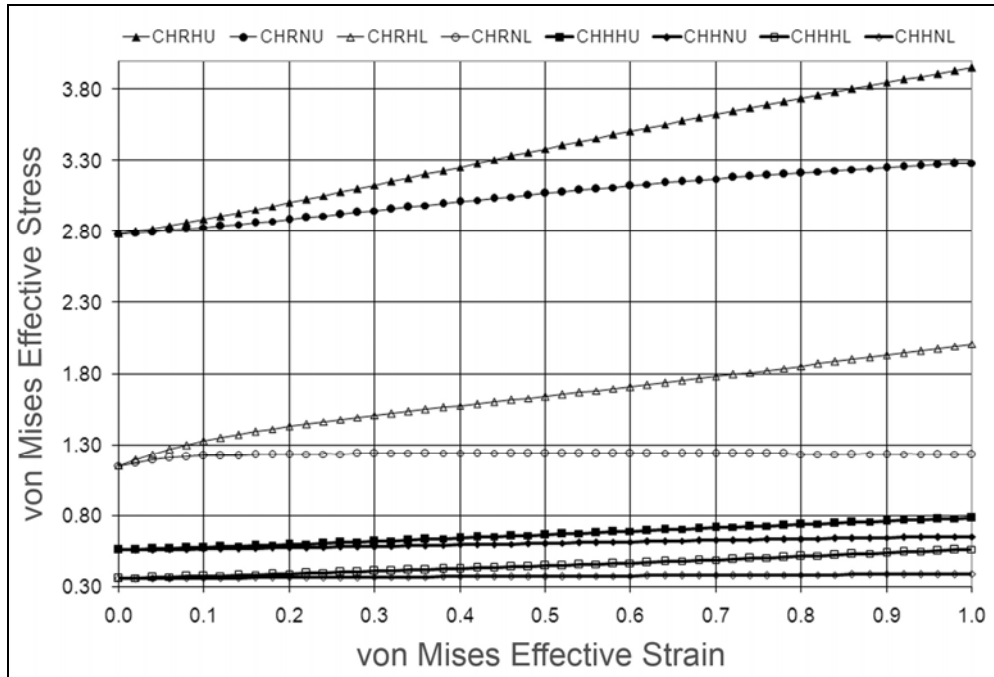


Figure 11. HCP Upper and Lower Bound Effective Stress-Strain Curves from C code

Figure 11 compares lower bound and upper bound SS curves for HCP material. Pole figures from the lower bound calculations are shown in Figure 12.

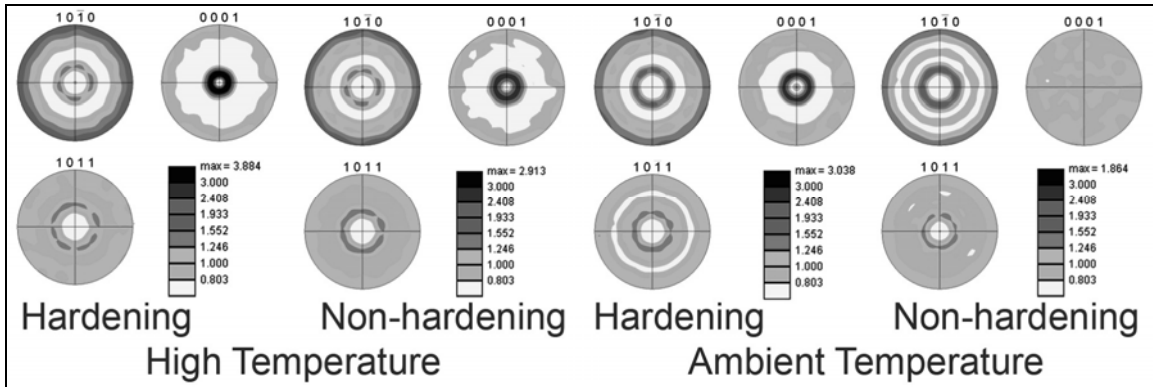


Figure 12. HCP Pole Figures for Lower Bound calculations with C code

Figure 13 compares SS results from the Affine and Taylor options of the V code.

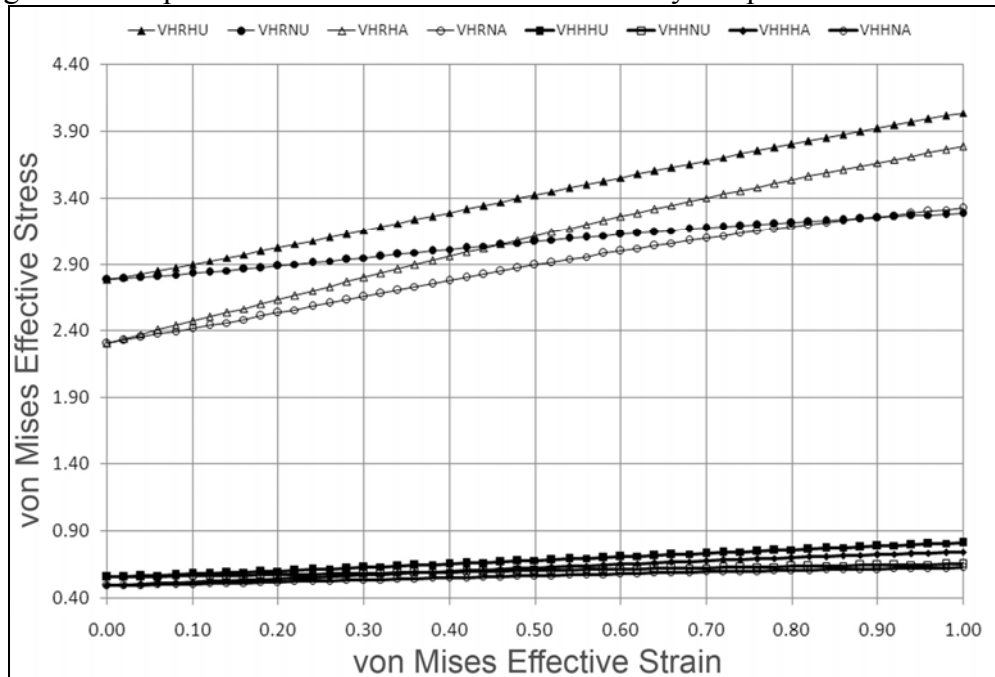


Figure 13. HCP Effective Stress-Strain Curves from Taylor and Affine options of V code

Pole figures obtained with the Affine option are shown in Figure 14.

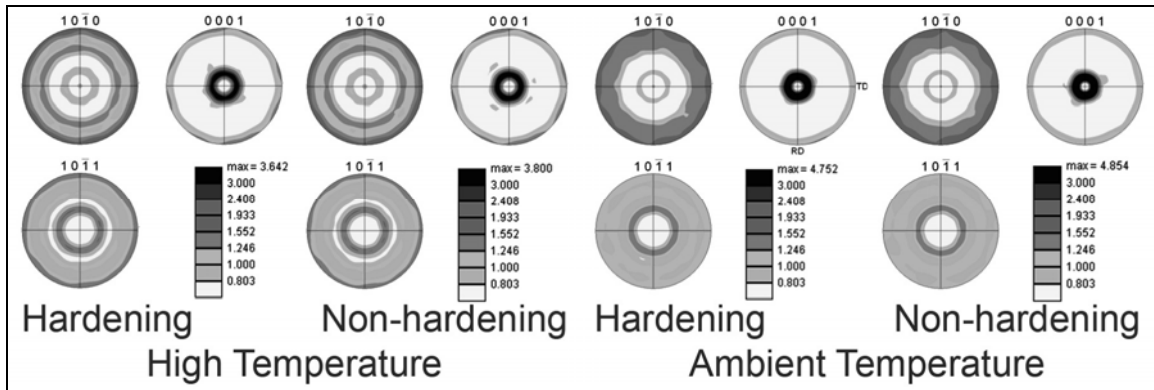


Figure 14. HCP Pole Figures from Affine option calculated with V code

DISCUSSION AND CONCLUSIONS

The ratio of initial flow stresses for the polycrystalline effective stress-strain curves under high and ambient temperature deformation conditions was nearly equal to the strain rate raised to a power $[(1/n_L) - (1/n_H)]$, where n_H and n_L refer to the stress exponents for high (H) and ambient (L) temperature deformation. Thus the difference in initial flow stresses is accentuated by the use of a relatively slow strain rate in the calculations. If the strain rate employed for the calculations were 1.0 s^{-1} , there would be virtually no difference in the initial flow stresses of the polycrystalline effective stress-strain curves obtained for the two deformation conditions. The differences that do exist can be attributed to a small amount of texture hardening.

Hardening exhibited by the effective stress-strain curves calculated using the Taylor assumption for the polycrystalline materials is virtually linear, as is the input constitutive equation. However, the intensity of hardening is enhanced in the polycrystalline aggregate as a result of texture formation. While the input hardening rates are $0.2(\text{CRSS})$ on each active slip system, the apparent linear hardening rates of the FCC polycrystal curves are 0.7 and 0.6 times the initial flow stress for the ambient and high temperature deformation conditions, respectively. The corresponding factors for the HCP polycrystal curves are 0.46 and 0.17. This enhanced hardening of the polycrystalline aggregate may also be attributed to texture hardening effects.

Texture differences between upper and lower bound calculations obtained with the C code can be attributed to two characteristics of the lower bound assumption: 1) in the lower bound approximation fewer grains accommodate more deformation in contrast to the upper bound where all grains experience the same deformation and 2) since all grains experience the same stress, hardening of a grain renders it less capable deforming further forcing other grains to accommodate more of the deformation. These effects cause the texture to be more strongly developed in the hardening cases for both high and low temperature deformation. With no hardening, all grains remain active and reorient as deformation progresses, while hardening causes decreased slip activity in some grains, forcing the activation of other grains.

All three codes produced excellent agreement among calculated effective stress-strain curves for all material and deformation conditions investigated. Pole figures produced by all codes were essentially identical for the Taylor homogenization hypothesis. The principal differences in pole figures for both FCC and HCP material occurred as a result of different strain-rate sensitivities.

ACKNOWLEDGEMENTS

One of the authors (CSH) wishes to acknowledge the support of the Materials Processing Group, Air Force Materials and Manufacturing Directorate for the conduct of the research.

REFERENCES

- ¹R. Lebensohn and C. Tomé, A self-consistent anisotropic approach for the simulation of plastic deformation and texture development of polycrystals – Application to zirconium alloys, *Acta Metall. Mater.*, **41**, 2611-2624 (1993).
- ²P.R. Dawson and E.B. Marin, Computational mechanics for metal deformation processes using polycrystal plasticity, *Advances in Applied Mechanics*, **34**, edited by E. van der Giessen and T. Y. Wu, Academic Press, 78–169 (1998).
- ³S. R. Kalidindi, C. A. Bronkhorst and L. Anand, Crystallographic Texture Evolution in Bulk Deformation Processing of FCC Metals, *J. Phys. Mech. Sol.*, **40**, 537-569 (1992).
- ⁴X. Wu, S. R. Kalidindi, C. Necker and A. A. Salem, Prediction of crystallographic texture evolution and anisotropic stress-strain curves during large plastic strains in high purity [alpha]-titanium using a Taylor-type crystal plasticity model, *Acta Mater.*, **55**, 423-432 (2007).
- ⁵R. A. Lebensohn, C. N. Tomé and P.J. Maudlin, A selfconsistent formulation for the prediction of the anisotropic behavior of viscoplastic polycrystals with voids, *J. Mech. Phys. Solids*, **52**, 249-278 (2004).
- ⁶B. L. Adams, S. I. Wright and K. Kunze, Orientation imaging: The emergence of a new microscopy, *Metall. Trans. A*, **24A**, 819-31 (1993).